Altermagnetic Flatband-Driven Fermi Surface Geometry for Giant Tunneling Magnetoresistance

Xingyue Yang, 1,2 Shibo Fang, 2 Zongmeng Yang, 1,2 Pin Ho, 3 Jing Lu, 1,4,5,6,7,8,* and Yee Sin Ang 2,†

1 State Key Laboratory for Mesoscopic Physics and School of Physics,

Peking University, Beijing 100871, P. R. China

2 Science, Mathematics and Technology (SMT) Cluster,

Singapore University of Technology and Design, Singapore 487372, Republic of Singapore

3 Quantum Innovation Centre (Q.InC), Agency for Science Technology

and Research (A*STAR), Singapore 138634, Republic of Singapore

4 Collaborative Innovation Center of Quantum Matter, Beijing 100871, P. R. China

5 Beijing Key Laboratory for Magnetoelectric Materials and Devices (BKL-MEMD),

Peking University, Beijing 100871, P. R. China

6 Peking University Yangtze Delta Institute of Optoelectronics, Nantong 226010, P. R. China

7 Key Laboratory for the Physics and Chemistry of Nanodevices,

Peking University, Beijing 100871, P. R. China

8 Beijing Key Laboratory of Quantum Devices, Peking University, Beijing 100871, P. R. China

Altermagnetism, characterized by zero net magnetization and symmetry-protected spin-split band structures, has recently emerged as a promising platform for spintronics. In altermagnetic tunnel junctions (AMTJs), the suppression of tunneling in the antiparallel configuration relies on the mismatch between spin-polarized conduction channels in momentum space. However, ideal nonoverlapping spin-polarized Fermi surfaces are rarely found in bulk altermagnets. Motivated by the critical influence of Fermi surface geometry on tunneling magnetoresistance (TMR), we investigate three experimentally synthesized altermagnets – bulk V_2Te_2O , RbV_2Te_2O , and KV_2Se_2O – to elucidate how flatband-driven Fermi surfaces minimize spin-channel overlap and boost AMTJ performance. Notably, RbV_2Te_2O and KV_2Se_2O host flat altermagnetic Fermi sheets, which confine spin degeneracy to minimal arc-like or nodal-like regions. Such Fermi surface geometry drastically reduces spin overlap, resulting in an unprecedented intrinsic TMR well over $10^3\%$ in the KV_2Se_2O -based AMTJ. Incorporating an insulating barrier further enhances the TMR to $\sim 10^5\%$, surpassing most conventional MTJs. These results not only establish KV_2Se_2O as a compelling candidate AMTJ material, but also highlight the critical role of flatband Fermi surface geometry in achieving high-performance altermagnetic-spintronic device technology.

I. INTRODUCTION

Magnetoresistive random-access memory (MRAM) is a promising candidate for next-generation nonvolatile memory technology, owing to its fast operation speed and low power consumption [1–4]. A magnetic tunnel junction (MTJ) forms the core of MRAM, which comprises two ferromagnetic (FM) electrodes separated by an insulating barrier [5–7]. In conventional MTJs, binary information is encoded in the relative magnetization alignment of the FM electrodes, while data writing and reading can be performed electrically through spin-transfer or spin-orbit torques [8, 9]. However, FM-based architectures suffer from stray magnetic fields, which limit device density and stability. Antiferromagnetic (AFM) materials inherently eliminate stray fields and exhibit ultrafast spin dynamics in the terahertz regime [10–12], but their compensated spin structure leads to negligible spin polarization in their band structures, which restricts their potential in spintronics.

Bridging the long-standing dichotomy between ferromagnetism and antiferromagnetism, altermagnetism has emerged as a compelling candidate for MRAM due to its "best-of-both-worlds" character: it features collinear AFM spin ordering together with FM-like spin-split electronic structures [13–15]. This unique combination enables spin-dependent transport in the absence of net magnetization, offering new opportunities for low-dissipation and high-speed spintronic applications. Unlike conventional antiferromagnets, altermagnets break both \mathcal{PT} (space inversion and time reversal) and $\mathcal{T}t$ (time reversal combined with half-cell translation) symmetries, leading to sizable nonrelativistic spin splitting away from high-symmetry paths in the Brillouin zone (BZ) [16, 17]. These features make altermagnets a compelling building block for MTJs, combining the spin-polarized transport of ferromagnets with the stray-field-free stability characteristic of antiferromagnets [10, 18–21].

Although multiple altermagnets have been theoretically proposed, their experimental realizations remain limited. Among the reported candidates, ${\rm RuO_2}$ remains one of the most extensively studied systems, but its altermagnetic nature is still under debate [22–26]. More recently, ${\rm KV_2Se_2O}$ [27, 28] and ${\rm RbV_2Te_2O}$ [29] have been experimentally confirmed to host d-wave altermagnetic band structures through spin- and angle-resolved photoemission spectroscopy (SARPES). Their above-room-temperature Néel temperatures and highly anisotropic

^{*} jinglu@pku.edu.cn

[†] yeesin_ang@sutd.edu.sg

spin-polarized Fermi surfaces [30] render them particularly attractive for altermagnet-based spintronic applications.

The transport characteristics and overall performance of an altermagnetic tunnel junction (AMTJ) are critically influenced by the Fermi surface geometry of its electrodes [30, 31]. The extent of spin matching (or mismatching) between spin-polarized conduction channels directly determines the current magnitude in the parallel (P) or antiparallel (AP) state, and hence the tunneling magnetoresistance (TMR) – a key figure of merit for MRAM technologies. Motivated by the pivotal role of Fermi surface geometry in shaping TMR, we examine three experimentally realized altermagnets – bulk V₂Te₂O, RbV₂Te₂O, and KV₂Se₂O – to elucidate how finite spinchannel overlap affects AMTJ behaviors. First-principles quantum transport simulations reveal that quasi-layered RbV₂Te₂O, and KV₂Se₂O possess only arc-like or nodallike intersections between opposite-spin channels, a direct consequence of their quasi-2D morphology, which hosts quasi-2D altermagnetic flatbands (or Fermi sheets) that drastically reduce the phase space for spin degeneracy. Such minimal overlaps strongly suppress the AP-state transmission, leading to large TMR ratios even in the absence of perfectly separated Fermi pockets.

In particular, KV₂Se₂O exhibits only four spindegenerate, nodal-like overlaps at the Fermi level, yielding an intrinsic TMR as high as $4.3 \times 10^3\%$ with a vacuum barrier. With an optimized insulating barrier, the TMR can be further increased to 9.1×10^4 %, exceeding the theoretical value of conventional Fe|MgO|Fe MTJs $(\sim 3700\%)$ by an order of magnitude [32, 33]. In contrast, when transport is oriented along a crystallographic direction with larger opposite-spin overlap, the TMR of the KV₂Se₂O AMTJ drops substantially to 3.3×10^3 %. These findings underscore the central role of Fermi surface engineering, particularly through altermagnetic flatband design and crystallographic orientation control, in achieving high-TMR AMTJs. This work not only reveals KV₂Se₂O as a compelling candidate for AMTJs, but also provides a blueprint for high-performance altermagnetic spintronic architectures, uniquely enabled by the spin-contrasting flatband Fermi-surface geometry of quasi-layered altermagnets.

II. RESULTS

A. Fermi Surface Geometry in Magnetic Tunnel Junctions

The transport properties of MTJs are governed by spin-dependent quantum tunneling across a thin insulating barrier. The efficiency of this process is strongly dictated by the Fermi surface geometry of the FM electrodes, which determines the momentum-resolved conduction channels available for tunneling (Figure 1) [34, 35]. In the ballistic regime, electron transmission

across the barrier requires the conservation of both spin and transverse momentum [36]. Because the Fermi surfaces of the FM electrodes are spin-polarized, the number of available conduction channels differs for majority and minority spins. As a result, the junction resistance depends sensitively on the relative magnetic alignment of the electrodes. When the magnetizations are parallel (P), the majority-spin channels on both sides align, vielding high conductance (low resistance). Conversely. in the antiparallel (AP) configuration, the strong mismatch between majority and minority spin bands significantly reduces the available tunneling pathways, leading to a high-resistance state. This resistance modulation via magnetic alignment leads to a TMR effect along all crystallographic directions in an FM-based MTJ [Figure 1(a)].

In the case of altermagnetic electrodes, strongly anisotropic, spin-polarized Fermi surfaces give rise to momentum-dependent and spin-contrasting conduction channels for opposite spins [17, 37]. When the Néel vectors of the two altermagnetic electrodes are antiparallel, the conduction channels become spin-mismatched, leading to a strong suppression of AP-state tunneling and thus producing a TMR effect [38]. For a typical planar d-wave Fermi surface geometry [Figure 1(b)], the rotational symmetry connecting opposite-spin sublattices enforces spin degeneracy at the Γ point, yielding a sizable number of spin-degenerate conduction channels. Consequently, AP-state transmission cannot be fully suppressed, and this residual "leakage" current limits the achievable TMR in such AMTJs.

Ideally, if the spin-resolved Fermi surfaces of the two electrodes exhibit no overlap at any transverse momentum [Figure 1(c)], transmission in AP state can be completely suppressed. C-paired spin-valley locking (SVL) in two-dimensional (2D) lattices provides a symmetry-driven route to realize such well-separated spin-polarized channels [39]. However, as interlayer coupling and the restoration of inversion symmetry in multilayer systems tend to hybridize opposite-valley spin states, SVL is typically realized in monolayer systems [40–43]. This makes direct implementation of SVL in AMTJs challenging, as stable vertical tunneling structures generally require bulk electrodes rather than monolayer components.

B. Candidate Altermangets for Magnetic tunnel Junctions

As fully separated spin-polarized pockets are rarely realized in three-dimensional (3D) bulk materials, we focus on more experimentally accessible cases of bulk AMs that host partially spin-degenerate conduction channels [44, 45]. Achieving large TMR in such systems requires Fermi surface geometries with minimal overlap between opposite-spin conduction channels. In particular, sufficiently flat Fermi surfaces can restrict this overlap to isolated, nodal-like spin-degenerate regions. Mo-

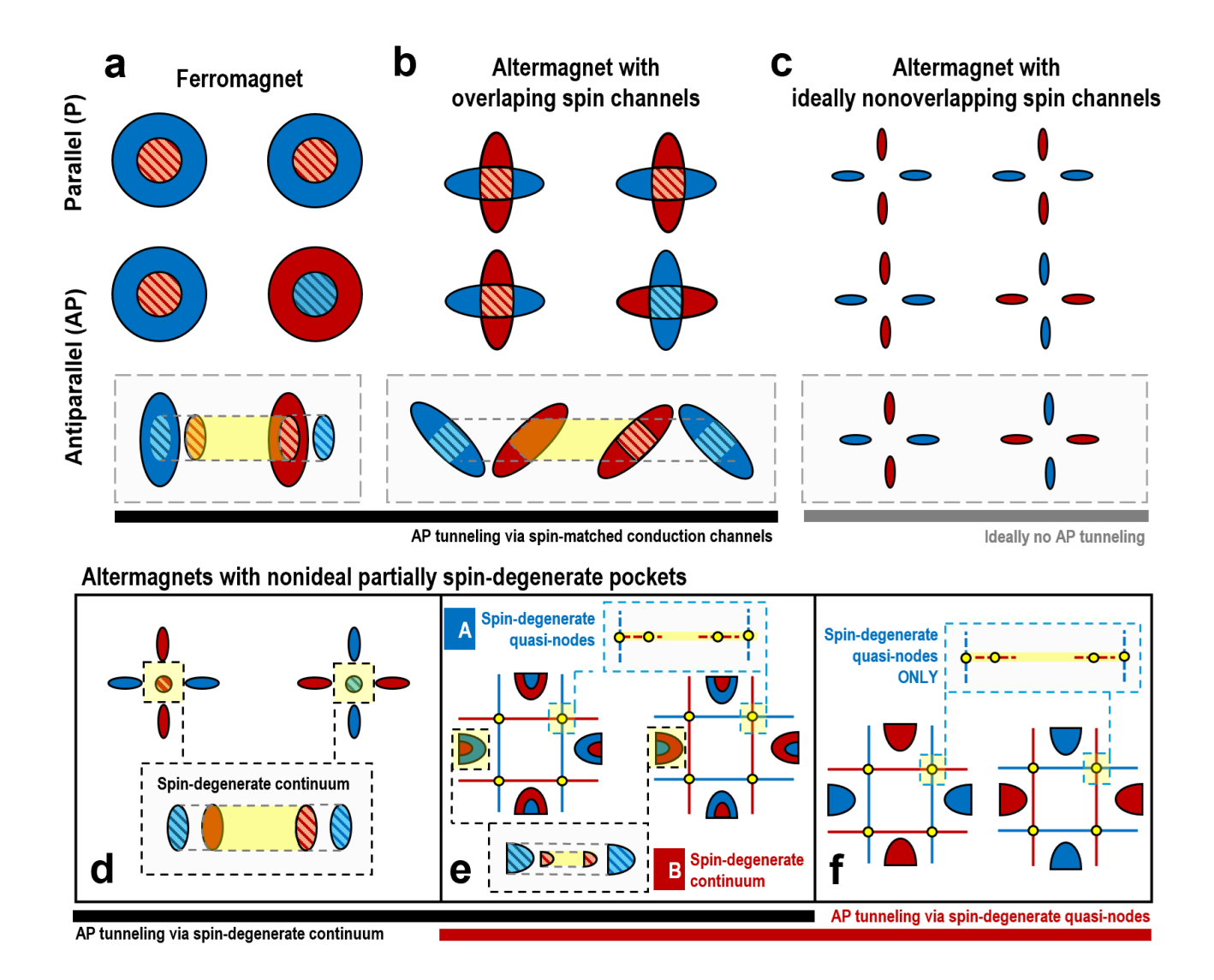


FIG. 1. Schematic illustration of tunneling magnetoresistance (TMR) mechanisms in MTJs with different electrode materials. a) Conventional ferromagnets. b) Typical altermagnets with overlapping spin conduction channels. c) AMs with ideally nonoverlapping spin conduction channels. (d-f) AMs with nonideal partially spin-degenerate Fermi pockets that allow residual AP tunneling. Two types of overlap are considered: spin-degenerate continuum and discrete spin-degenerate quasi-nodes. Red and blue denote spin-up and spin-down conduction channels, respectively.

tivated by this consideration, we examine three experimentally synthesized layered altermagnetic candidates – bulk V_2Te_2O [46], RbV_2Te_2O [29] and KV_2Se_2O [27] – each of which hosts highly anisotropic, band-flattened Fermi surfaces. As illustrated in Figures 1(d–f), these systems exhibit distinct forms of residual overlap, ranging from extended spin-degenerate continua to discrete spin-degenerate quasi-nodes. In the following, we systematically investigate their structural and electronic characteristics (see Figure 2) to assess their suitability for AMTJ device applications.

Monolayer $V_2\mathrm{Te}_2\mathrm{O}$ exhibits a tetragonal lattice with a checkerboard configuration [Figure 2(a)]. Each vanadium atom is coordinated by four Te and two O atoms in a distorted octahedral environment, and exhibits stag-

gered out-of-plane magnetization. In the multilayer form, V₂Te₂O adopts an AB-AFM stacking, where adjacent layers are laterally shifted by half a unit cell and alternate in spin orientations [46]. Structurally, the two opposite-spin sublattices are not related by spatial inversion or translation, but are instead connected by C_{4z} or $M_{1\bar{1}0}$ operation. This symmetry arrangement gives rise to a planar d-wave altermagnetic order, which is reflected in its spin-split band structures. The energy bands along the $\Gamma-X-M$ and $\Gamma-Y-M$ paths exhibit opposite spin splitting [Figure 2(c)], whereas those along the $\Gamma-M$ path remain spin-degenerate. This momentum-dependent spin texture results in discrete spin-polarized Fermi pockets near the X and Y valleys, whereas multiple band crossings near the Γ point generate an extended

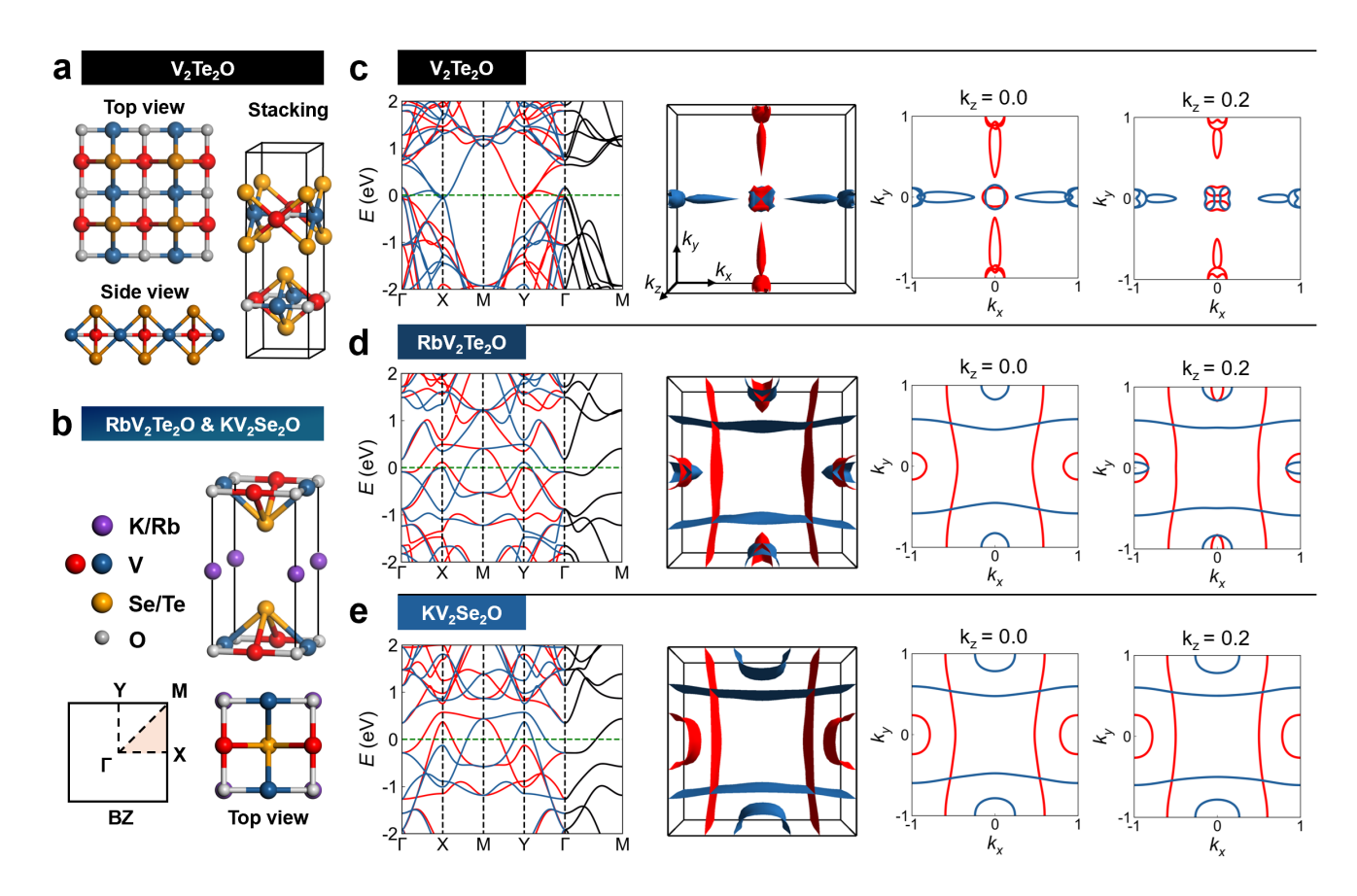


FIG. 2. Crystal and magnetic structures of a) V_2Te_2O , b) RbV_2Te_2O and KV_2Se_2O . Red and blue indicate up and down spins of the V atoms, respectively. (c-e) Electronic band structures, three-dimensional spin-resolved Fermi surfaces and Fermi surface cross-sections at different k_z planes ($k_z = 0$ and 0.2) of different materials. Spin-degenerate bands are shown in black.

spin-degenerate continuum at the Fermi level.

RbV₂Te₂O and KV₂Se₂O are experimentally confirmed metallic d-wave alternagnets [27, 29]. These altermagnets share an identical layered structure, consisting of V₂Te(Se)₂O sheets separated by Rb/K atoms [Figure 2(b)]. They crystallize in a tetragonal lattice with space group P_4/mmm . Nuclear magnetic resonance measurements reveal staggered spin orientations of V atoms along the c axis within each V_2 Te(Se)₂O plane, with a Néel temperature well above room temperature. The magnetic structure also breaks both \mathcal{PT} and $\mathcal{T}t$ symmetries, while preserving combined symmetries such as $[C_2||C_{4z}]$ and $[C_2||M_{1\bar{1}0}]$ (the left operation acting in spin space while the right acting in real space). These symmetry characteristics produce spin-split patterns analogous to those of bulk V₂Te₂O [Figures 2(d,e)]. The spin-resolved Fermi surfaces of both compounds consist of quasi-2D sheets extending along k_z , with distinct pockets near the Brillouin zone (BZ) boundaries. Due to the intercalation of Rb/K atoms, the interlayer distance in RbV₂Te₂O and KV₂Se₂O (7.47 Å) is significantly larger than in multilayer V₂Te₂O (6.38 Å), leading to nearly-flat Fermi surface sheets. A comparison of the $k_z = 0.2$ Fermi surface cross-sections reveals that ${\rm RbV_2Te_2O}$ retains arclike regions of residual overlap, while $\mathrm{KV_2Se_2O}$ achieves nearly complete spin separation, with only four spin-degenerate nodal points. The presence of such minimal spin-degenerate regions suggests strong suppression of AP-state leakage current and, consequently, large TMR in these altermagnetic systems.

C. Intrinsic transport properties of V_2Te_2O , RbV_2Te_2O and KV_2Se_2O AMTJs

Having established the Fermi surface geometries of the three representative bulk altermagnets, we now turn to their intrinsic transport properties along the [001] direction. As a preliminary assessment, the AMTJs are modeled using an ideal 6Åvacuum spacer [Figure 3(a)]. Such modelling setup enables a more direct assessment on how Fermi surface geometry inherent to each material influences the resulting TMR performance, before addressing the complicated interfacial effects when an insulating barrier is employed. Figures 3(b-d) show the transversemomentum (k_{\parallel}) -resolved transmission coefficients at the Fermi level for spin-up and spin-down electrons. In the P state, the transmission profiles closely resemble the pro-

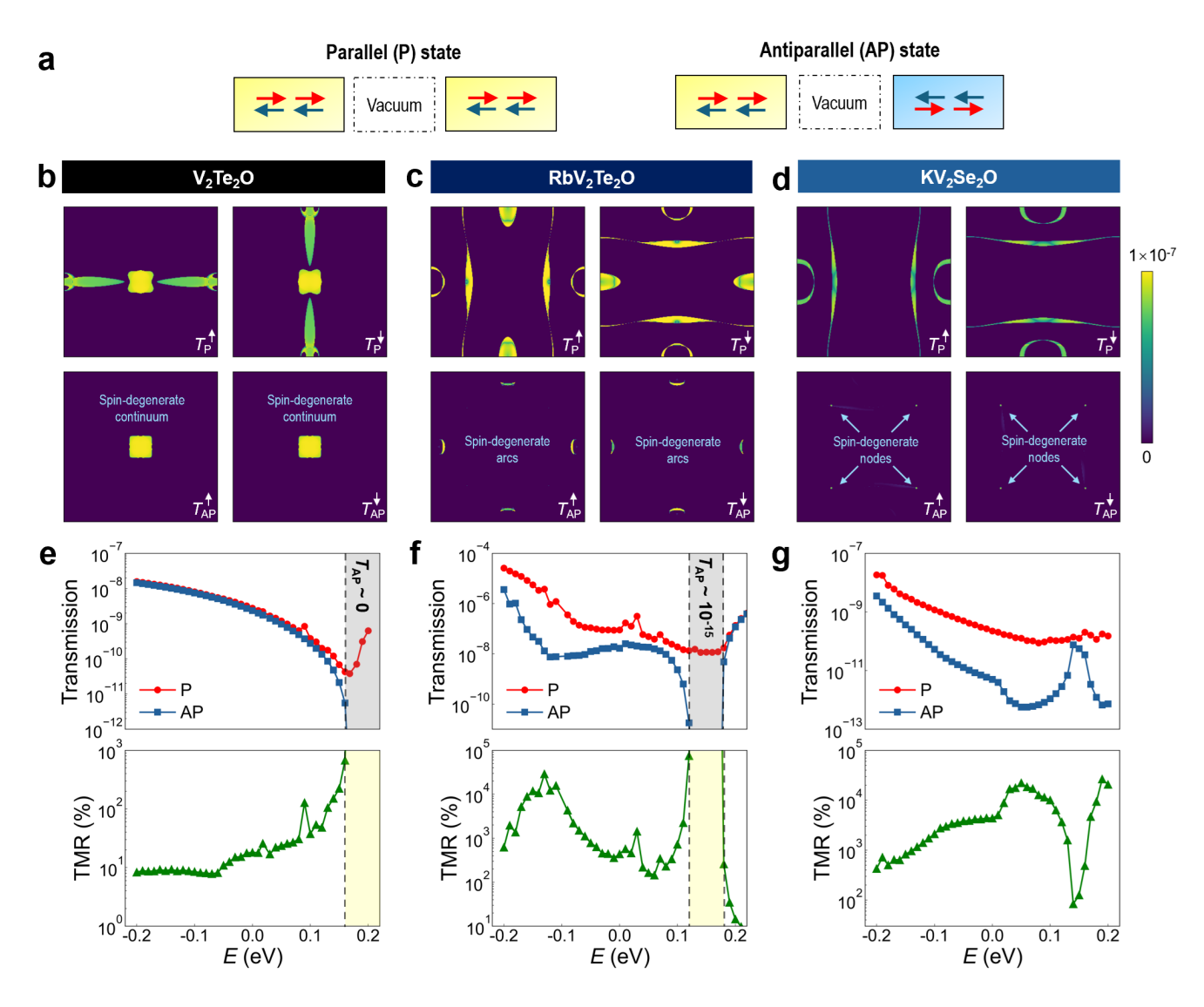


FIG. 3. Intrinsic transport properties of AMTJs with vacuum barriers based on V_2Te_2O , RbV_2Te_2O and KV_2Se_2O electrodes. a) Schematic illustration of magnetization alignments in the parallel (P) and antiparallel (AP) configurations. (b-d) Calculated spin-resolved, k_{\parallel} -resolved transmission coefficients at the Fermi level for each AMTJ in both P and AP states. (e-g) Energy-dependent total transmission spectra for P and AP states, along with the resulting TMR ratio. Shaded regions highlight the energy ranges where AP tunneling $T_{\rm AP}$ is significantly suppressed due to changes in available conduction channels when energy is away from the Fermi level.

jections of the anisotropic Fermi surfaces onto the [001] plane, as the spin-matched bands of the two electrodes generate efficient conduction channels. In contrast, electron transmission in the AP state is strongly suppressed throughout the BZ, except in several regions where spins are degenerate, namely (i) an extended continuum for V_2Te_2O [Figure 3(b)]; (ii) arc-like features for RbV₂Te₂O [Figure 3(c)]; and (iii) nodal-like features for KV₂Se₂O [Figure 3(d)].

The V_2Te_2O -based AMTJ exhibits pronounced transmission features for both spin channels in the P state, as characterized by a broad high-intensity region centered at the Γ point and extended continua along the $-X-\Gamma-X$ or $-Y-\Gamma-Y$ direction. The spin-up and spin-down trans-

mission patterns share identical geometries, differing only by a $\pi/2$ rotation, which is consistent with the d-wave symmetry of the altermagnetic order. Consequently, the total current along the [001] direction remains effectively spin-neutral. Owing to the large spin-degenerate continuum around the Γ point, AP-state tunneling cannot be completely suppressed, giving rise to a residual leakage current. As a result, the AMTJ yields a modest TMR of only 18% at $E_{\rm F}$.

The evolution of the total transmission with energy further reveals the underlying mechanism [Figure 3(e)]. In both configurations, the transmission initially decreases with increasing energy. Beyond E > 0.16 eV, however, the total transmission in the P state $T_{\rm P}$ ($T_{\rm P} =$

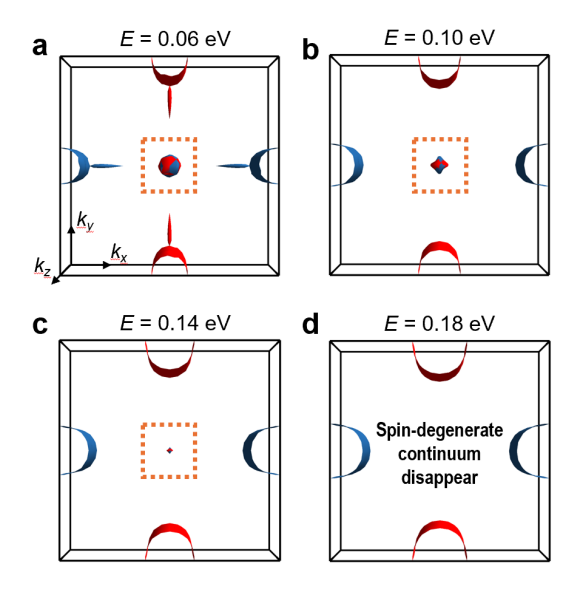


FIG. 4. Three-dimensional Fermi surfaces of bulk V₂Te₂O at a) E=0.06 eV, b) E=0.10 eV, c) E=0.14 eV and d) E=0.18 eV. Red and blue indicate spin-up and spin-down Fermi surfaces, respectively. The spin-degenerate continuum near the Γ point progressively diminishes with increasing energy and entirely vanishes at E=0.18 eV.

 $T_{\rm P}^{\uparrow} + T_{\rm P}^{\downarrow}$) exhibits a sharp increase while $T_{\rm AP}$ drops abruptly to nearly zero (shaded region). This sudden contrast originates from the evolution of the bulk $V_2 Te_2 O$ Fermi surfaces at higher energies. As illustrated in Figure 4, increasing the energy from 0.06 to 0.18 eV progressively reduces the spin-degenerate continuum near the Γ point, which eventually disappears at E=0.18 eV. At this energy, $V_2 Te_2 O$ becomes an ideal electrode material for AMTJs, exhibiting perfectly separated spin-polarized conduction channels. The Fermi surface geometry thus plays a crucial role in optimizing the device performance of AMTJ.

In contrast to V_2Te_2O , the Fermi surface geometries of RbV_2Te_2O and KV_2Se_2O exhibit no overlap near the Γ point [Figures 3(c,d)]. Both AMTJs feature narrow transmission channels in the P state, with distinct Fermi pockets at the BZ boundary, which is consistent with their quasi-2D altermagnetic nature. However, the spin-polarized pockets in RbV_2Te_2O are not completely separated, giving rise to several extended spin-degenerate "arcs" that sustain AP transmission. By contrast, the KV_2Se_2O -based AMTJ hosts only four discrete, "nodal-like" intersection points between opposite-spin conduction channels. These isolated nodes, providing minimal conduction pathway, immediately suggest a strong suppression of AP-state tunneling in the device.

The distinction between the spin-degenerate "arcs" in RbV_2Te_2O and the discrete "nodal points" in KV_2Se_2O is quantitatively reflected in their total transmission spectra and the corresponding TMR ratios [Figure 3(f,g)]. In RbV_2Te_2O , the persistence of spin-degenerate "arcs" leads to a moderate TMR ratio of 435% at the Fermi

level. In contrast, the $\mathrm{KV_2Se_2O}$ -based AMTJ exhibits a pronounced difference between the P- and AP-state transmissions at E_F , resulting in a much higher TMR of $4.3 \times 10^3\%$. The shaded region in Figure 3(f) highlights a reduction in AP tunneling for $\mathrm{RbV_2Te_2O}$, which can be attributed to subtle changes in its Fermi surface geometry (see Section B of the Supporting Information for details).

Taken together, the contrasting forms of the spin-degenerate regions – continua in $V_2 Te_2 O$, arcs in $RbV_2 Te_2 O$, and discrete nodal points in $KV_2 Se_2 O$ – together with their corresponding order-of-magnitude variations in the TMR, underscore the pivotal role of Fermi-surface overlap in determining and pushing the performance limits of AMTJs.

D. Tunneling magnetoresistance of KV_2Se_2 -based AMTJ with insulating spacers

Having identified KV₂Se₂O as the most promising electrode material with intrinsically high TMR at the Fermi level, we next investigate its performance in more realistic device architectures that incorporate an insulating barrier. The choice of barrier can critically influence both tunneling efficiency and spin selectivity, as its electronic structure and symmetry compatibility with the electrodes directly affect the available tunneling pathways [47]. For instance, by exploiting the spin-filtering effect in altermagnetic semiconductors, a sizable TMR can also be realized in AM-barrier MTJs [48–50]. An appropriately chosen barrier can therefore substantially enhance the achievable TMR ratio beyond the intrinsic limit imposed by the electrode Fermi surface. To this end, we construct KV₂Se₂O-based AMTJs incorporating realistic barrier materials along the [001] and [100] directions, and systematically evaluate their transport characteristics.

For transport along the [001] direction, we select Cr₂Se₂O as the tunnel barrier due to its structural compatibility with KV₂Se₂O and a lattice mismatch below 1%. In its monolayer (ML) form, Cr₂Se₂O is a twodimensional altermagnet [51, 52], exhibiting staggered spin orientations on neighboring Cr atoms with magnetic moments perpendicular to the atomic plane [Figure 5(a) [51, 53]. Owing to its structural similarity to ML V₂Te₂O, this material also displays planar d-wave altermagnetism, as reflected in its band structure [Figure 5(b)], with a band gap of 1.12 eV. We examine three possible stacking configurations for multilayer Cr₂Se₂O and identify the AB-AFM arrangement as the most stable one (see Section C of the Supporting Information for details). This configuration exhibits a substantially reduced band gap of 0.26 eV compared with the monolayer. Four Cr₂Se₂O layers are employed to separate the electrodes. The layer-resolved density of states (LDOS) of the AMTJ reveals a well-defined gap at the Fermi level within the barrier region [Figure 5(c)], thus confirming that the four-

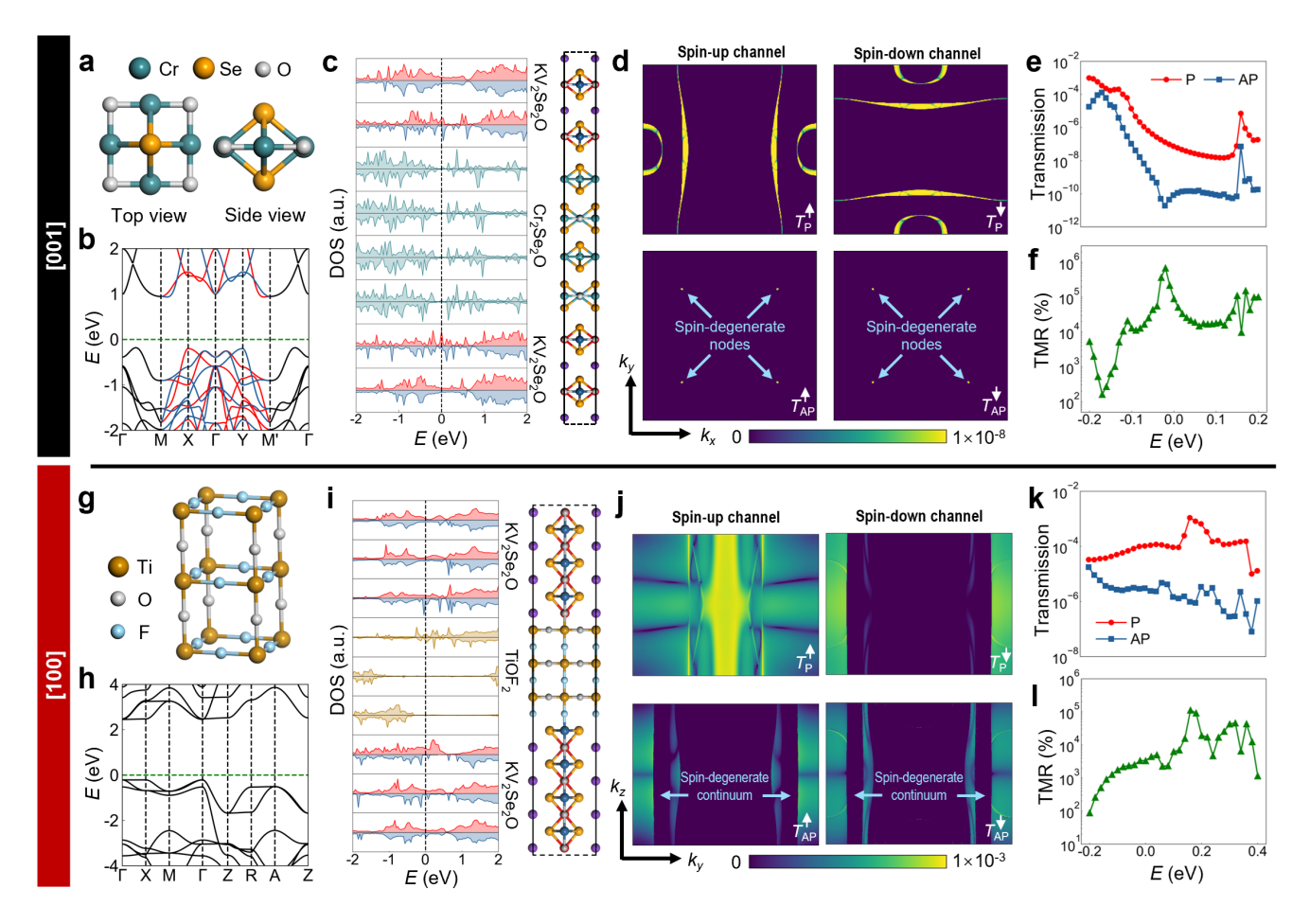


FIG. 5. Transport properties of KV_2Se_2O -based AMTJs along the (a-f) [001] and (g-i) [100] directions. a) Crystal structure of the barrier material Cr_2Se_2O . b) Electronic band structures of monolayer Cr_2Se_2O , where red and blue denote spin-up and spin-down bands, respectively; spin-degenerate bands are shown in black. c) Atomic structure and layer-resolved density of states (LDOS) of the $KV_2Se_2O|Cr_2Se_2O|KV_2Se_2O|(001)$ MTJ. Each panel corresponds to a single atomic layer of either KV_2Se_2O or Cr_2Se_2O , with spin-up and spin-down components shown in the upper and lower subpanels. The Fermi level is marked by a dashed line. d) k_{\parallel} -resolved spin-polarized transmission coefficients at the Fermi level for the (001) AMTJ in both P and AP states. e) Total transmission spectra and f) TMR ratio as a function of energy. (g-l) Same as (a-f) but for the $KV_2Se_2O|TiOF_2|KV_2Se_2O|MTJ$ along the [100] direction.

layer barrier effectively decouples the Bloch states of the two electrodes and ensures tunneling-dominated transport.

Depending on the specific magnetization configuration of Cr_2Se_2O , the (001) AMTJ can adopt four distinct magnetic states, denoted as $P/AP_{1/2}$ [Figure S4]. Here, P(AP) corresponds to the parallel (antiparallel) alignment between the two KV_2Se_2O electrodes, while the subscript 1 or 2 specifies whether the Néel vector of the leftmost Cr_2Se_2O layer is parallel or antiparallel to that of the left electrode. Because adjacent Cr_2Se_2O layers are laterally shifted by half a unit cell, these configurations are not equivalent in their transport characteristics (see Section D of the Supporting Information for details). Our calculations show that the P_1/AP_1 pair yields a higher TMR ratio at the Fermi level compared with P_2/AP_2 . Therefore, in the following discussion, the P_1 and AP_1 states are taken as the representative parallel and

tiparallel configurations, respectively.

The k_{\parallel} -resolved transmission coefficients for the KV₂Se₂O-based AMTJ along the [001] direction are shown in Figure 5(d). The transmission patterns in the P state closely resemble those of the intrinsic (vacuumbarrier) case, while the nodal-like features remain well preserved in the AP configuration. The total transmission in the P state increases by nearly two orders of magnitude compared with the vacuum-barrier junction [Figure 5(e)], whereas the change in the AP-state transmission is much smaller. Specifically, $T_{\rm P}$ rises from 2.2×10^{-10} to 7.5×10^{-8} , while $T_{\rm AP}$ increases only from 5.0×10^{-12} to 8.2×10^{-11} at the Fermi level. These results underscore the crucial role of barrier material in further optimizing the TMR effect. Consequently, a giant TMR ratio of $9.1 \times 10^4\%$ is achieved at $E_{\rm F}$ – over two orders of magnitude higher than the previously reported value of $\sim 500\%$ in RuO₂|TiO₂|RuO₂ AMTJs [19].

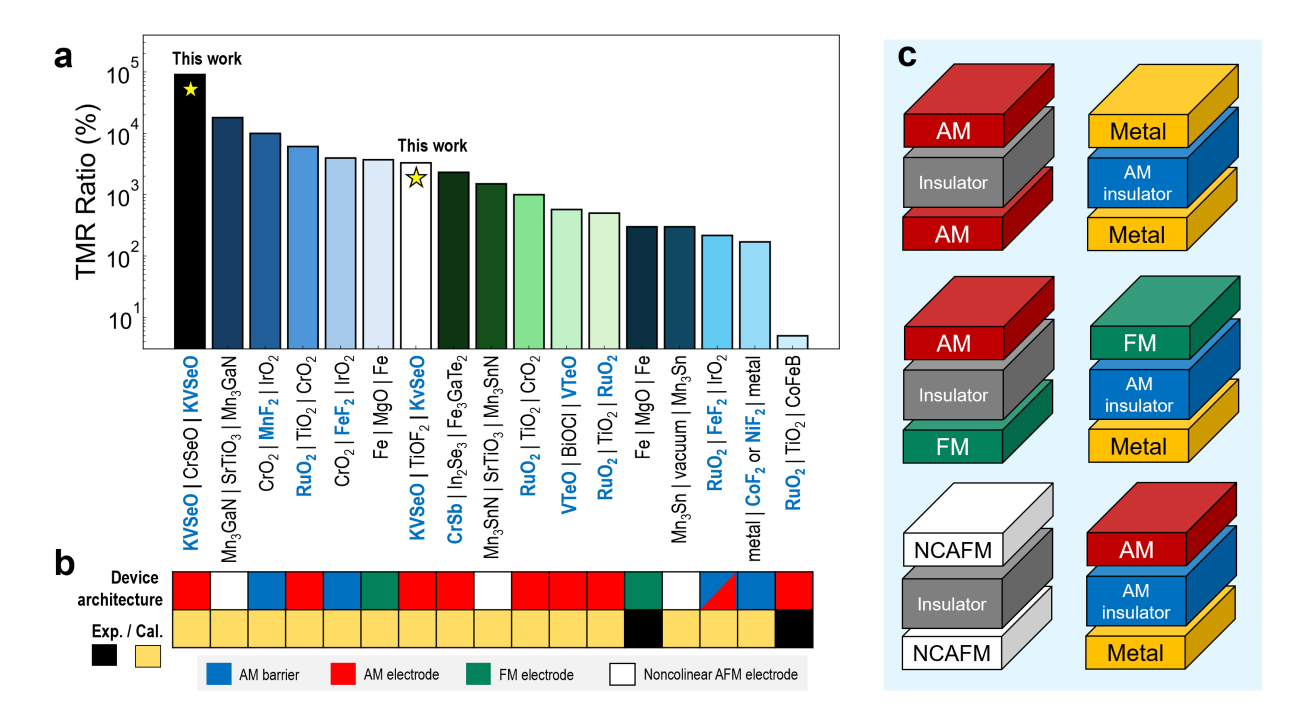


FIG. 6. Benchmark of MTJ performances. a) Comparison of TMR ratios obtained using KV_2Se_2O (abbreviated as KVSeO) electrodes in this work (highlighted with stars) and selected results from recent experimental and theoretical studies [19, 23, 32, 33, 48, 49, 54–62]. Altermagnetic materials are marked with blue. For simplicity, KV_2Se_2O and Cr_2Se_2O are abbreviated as KVSeO and CrSeO, respectively. Since the altermagnetism of Cr_2Se_2O does not play a decisive role in the TMR of the KV_2Se_2O (001) device, we do not emphasize its altermagnetic nature here. b) Device architectures and methodology (experimental or computational) corresponding to each bar in panel (a). The top row codes the type of functional layer – AM barrier, AM electrode, FM electrode or noncollinear AFM electrode, while the bottom row distinguishes between experiment (Exp.) and calculation (Cal.). c) Schematic illustrations of representative MTJ architectures.

E. Crystal facet engineering in KV_2Se_2 -based AMTJ

Due to the pronounced anisotropy of the Fermi surface in KV₂Se₂O, its transport characteristics exhibit strong directional dependence. When the current flows along the [100] direction, the symmetry constraints ($[C_2||C_{4z}]$) responsible for spin neutrality in the [001] orientation are lifted, resulting in spin-polarized transport analogous to that in conventional FM-based MTJs. To ensure structural compatibility and minimize lattice strain, the semiconductor TiOF₂ is chosen as the insulating barrier. The atomic and electronic structures of TiOF₂ are shown in Figures 5(g,h). TiOF₂ crystallizes in a tetragonal lattice and exhibits an excellent lattice match with KV₂Se₂O (mismatch < 1%). Furthermore, TiOF₂ possesses a wide band gap of 2.67 eV, which remains well preserved in the KV₂Se₂O|TiOF₂|KV₂Se₂O (100) heterostructure [Figure 5(i)].

The transmission along the [100] direction [Figure 5(f)] exhibit distinct patterns compared with that along [001]. For spin-up electrons, the quasi-2D Fermi surface sheets extended along $k_z - k_y$ plane form continuous conduction channels throughout the BZ, resulting in a relatively high transmission. In contrast, the spin-down Fermi sheets, oriented primarily along the k_z - k_x plane,

have only limited projection onto the [100] transport plane. Consequently, $T_{\rm P}^{\downarrow}$ is dominated by isolated spin-down Fermi pockets located near $k_{\rm y}=\pm\pi/a$. In the AP configuration, the number of available transmission states is markedly reduced, with tunneling restricted to small regions near the Brillouin zone boundaries where the spin-down pockets overlap with the opposite-spin Fermi sheets. The resulting spin polarization, defined as $p=(T^{\uparrow}-T^{\downarrow})/(T^{\uparrow}+T^{\downarrow})$, reaches 73.2% when the Néel vectors of the KV₂Se₂O electrodes are aligned.

By integrating over k_{\parallel} , we obtain the total transmission spectra and corresponding TMR ratio as functions of energy [Figures 5(k,l)]. Because both the P and AP configurations host a larger number of available conduction channels, the overall transmission along the [100] direction is substantially enhanced. At the Fermi energy, the TMR reaches $3.3 \times 10^3\%$, which is much smaller than that of the [001] device due to the spin-degenerate continua that yield sizable AP-state tunneling. Here, [100] configurations have the advantage of overall larger transmission value in the P states, hence better signal-to-noise ratio during device readout [63], but this comes at the cost of a reduced TMR relative to the [001] counterpart. The pronounced contrast between the [001] and [100] configurations thus underscores the crystal facet engineering in tailoring the performance metrics of AMTJs.

F. Performance Benchmarking

We provide a performance benchmark of KV_2Se_2O -based AMTJs in Figure 6. We compare their TMR ratios with representative experimental and theoretical results from recent MTJ studies [Figs. 6a,b; see Section E of the Supporting Information for details] under different device configurations [see Figure 6(c) for representative MTJ setups]. Conventional FM MTJs, such as Fe|MgO|Fe, typically yield theoretical TMR values around 3700% [57], whereas experimental measurements are limited to 180-300% [32, 33]. In comparison, the simulated TMR ratios for RuO₂-based AMTJs remain on the order of $10^3\%$ [19, 56, 60].

Notably, our proposed KV₂Se₂O|Cr₂Se₂O|KV₂Se₂O [001] device achieves a record-high TMR of $9.1 \times 10^4\%$, surpassing all previously reported AMTJs here by more than an order of magnitude. This exceptional performance originates from the combination of: (i) the altermagnetic flatband Fermi surface geometry of KV₂Se₂O which yields minimal nodal-like conduction channels in the AP state; combined with (ii) the symmetry-matched Cr₂Se₂O insulating barrier. When transport occurs along the [100] direction, the TMR is substantially reduced due to the presence of extended spin-matched conduction channels in the AP configuration – though the resulting TMR remains comparable to many other MTJ designs. Overall, our computational results establish the theoretical performance ceiling of KV₂Se₂O-based AMTJs, providing both a quantitative benchmark for material selection and a conceptual framework for the Fermi-surface-engineered design of next-generation spintronic devices.

III. CONCLUSION

In summary, we have systematically investigated the intrinsic transport characteristics in AMTJs using three experimentally realized bulk altermagnets - V₂Te₂O, RbV₂Te₂O, and KV₂Se₂O. We demonstrated that the degree of overlap between opposite-spin conduction channels serves as the key factor governing the TMR performance. Among these materials, KV₂Se₂O exhibits nearly nodal-like spin-degenerate conduction channels in the AP state, which arises from its altermagnetic flatband Fermi surface geometry. As a result, an intrinsic TMR of $4.3 \times 10^3\%$ was obtained, which was further enhanced to $9.1 \times 10^4\%$ by employing a symmetrymatched Cr₂Se₂O insulating barrier in an AMTJ device setup. The pronounced contrast between the [001] and [100] transport directions underscores the essential role of Fermi surface geometry engineering via crystallographic orientation, which enables the overall magnitude of the transmission and the TMR to be tuned and balanced depending on the application needs.

Beyond identifying KV₂Se₂O as a compelling altermagnetic electrode material, our results revealed the pivotal role of altermagnetic flatbands in achieving ultrahigh-TMR AMTJs with minimal spin-degenerate "arc-" or "node-" like conduction channels. More broadly, this work established a concrete design principle for altermagnetic-spintronic devices: high-performance AMTJs are enabled when quasi-layered altermagnets hosting flatband-driven, symmetry-protected Fermi surface geometries that minimize opposite-spin overlap. This flatband-centric paradigm provides a powerful materials design and screening guideline and paves a pathway toward next-generation altermagnetic-spintronics uniquely empowered by quasi-layered altermagnets.

IV. EXPERIMENTAL SECTION

A. Density Functional Theory Simulations

The geometry optimization and electronic structure calculations for V₂Te₂O, RbV₂Te₂O and KV₂Se₂O are carried out using the Vienna Ab initio Simulation Package (VASP) [64, 65]. The projector augmented wave (PAW) method is employed, with the exchange-correlation effects treated within the generalized gradient approximation (GGA) using the Perdew-Burke-Ernzerhof (PBE) functional [66]. We set the plane-wave cutoff energy to 600 eV and sample the Brillouin zone with a dense Monkhorst-Pack grid of $25 \times 25 \times 13$. The atomic positions are relaxed until the residual forces on each atom are less than 10^{-2} eV/Å. The on-site Coulomb interaction is treated within the GGA+U scheme [67, 68], with $U_{\text{eff}} = 3.7 \text{ eV}$ on V 3d orbitals for V₂Te₂O [46] and 1.0 eV for RbV₂Te₂O [29]. We do not apply a Hubbard U correction when calculating KV₂Se₂O, as our tests [see Section A of the Supporting Information for details] show that this setting yields band structures most consistent with the experimental SARPES results [27]. To minimize lattice mismatch and the associated structural distortion, we employ Cr₂Se₂O and TiOF₂ as the tunnel barriers for the KV₂Se₂O AMTJ along the [001] and [100] directions, respectively. Hubbard U corrections for the above two compounds are 3.5 eV on Cr 3d orbitals [51] and 4.2 eV on Ti 3d orbitals

B. Quantum Atomistic Device Simulations

The spin-dependent transport properties are evaluated using Density Functional Theory (DFT) combined with the nonequilibrium Green's function (NEGF) formalism, implemented in the ATK package [70, 71]. Our device is modeled as a two-probe system, consisting of a central region and two electrodes. The spin-resolved transmission coefficient $T_{k_{\parallel},s}(E)$ can be written as

$$T_{k_{\parallel},s}(E) = \text{Tr}[G_{k_{\parallel},s}(E)\Gamma^l_{k_{\parallel},s}(E)G_{k_{\parallel},s}(E)^{\dagger}\Gamma^r_{k_{\parallel},s}(E)]$$

where k_{\parallel} denotes the reciprocal lattice vector parallel to the electrode interface (orthogonal to the transport direction) in the irreducible Brillouin zone, and s labels the spin. Here, $G_{k_{\parallel},s}(E)$ is the retarded Green's function for spin s at k_{\parallel} , while $\Gamma_{k_{\parallel},s}^{l(r)}(E)$ denotes the broadening function of the left (right) electrode, which equals the imaginary part of the corresponding self-energy term [72]. The AMTJ simulations employ a density mesh cutoff of 180 Hartree and an electronic temperature of 300 K. The Brillouin zone is sampled using k-point meshes of $23 \times 23 \times 1$ and $23 \times 13 \times 1$ for devices oriented along the [001] and [100] directions, respectively. To accurately describe the van der Waals interaction in V₂Te₂O multilayers, Grimme's DFT-D3 correction is applied [73].

ACKNOWLEDGMENTS

This work is supported by the National Natural Science Foundation of China (No. 12274002 and 91964101), the Ministry of Science and Technology of China (No. 2022YFA1203904), the Fundamental Research Funds for the Central Universities, and the High-performance Computing Platform of Peking University. Y.S.A. acknowledges the supports from the Kwan Im Thong Hood Cho Temple Early Career Chair Professorship in Sustainabiltiy, and the Ministry of Education, Singapore, Academic Research Fund Tier 2 under the award number MOE-T2EP50224-0021.

- [1] D. C. Worledge and G. Hu, Spin-transfer torque magnetoresistive random access memory technology status and future directions, Nature Reviews Electrical Engineering 1, 730 (2024).
- [2] S. Jung, H. Lee, S. Myung, H. Kim, S. K. Yoon, S.-W. Kwon, Y. Ju, M. Kim, W. Yi, S. Han, et al., A crossbar array of magnetoresistive memory devices for in-memory computing, Nature 601, 211 (2022).
- [3] A. Sharma, A. A. Tulapurkar, and B. Muralidharan, Proposal for energy efficient spin transfer torquemagnetoresistive random access memory device, Journal of Applied Physics 129 (2021).
- [4] C. Chappert, A. Fert, and F. N. Van Dau, The emergence of spin electronics in data storage, Nature materials 6, 813 (2007).
- [5] M. Julliere, Tunneling between ferromagnetic films, Physics letters A 54, 225 (1975).
- [6] B. Jinnai, K. Watanabe, S. Fukami, and H. Ohno, Scaling magnetic tunnel junction down to single-digit nanometers—challenges and prospects, Applied physics letters 116 (2020).
- [7] Y. Zhang, W. Sun, K. Cao, X.-X. Yang, Y. Yang, S. Lu, A. Du, C. Hu, C. Feng, Y. Wang, et al., Electric-field control of nonvolatile resistance state of perpendicular magnetic tunnel junction via magnetoelectric coupling, Science Advances 10, eadl4633 (2024).
- [8] I. Žutić, J. Fabian, and S. D. Sarma, Spintronics: Fundamentals and applications, Reviews of modern physics 76, 323 (2004).
- [9] Z. Zheng, L. Jia, Z. Zhang, Q. Shen, G. Zhou, Z. Cui, L. Ren, Z. Chen, N. F. Jamaludin, T. Zhao, et al., Allelectrical perpendicular switching of chiral antiferromagnetic order, Nature Materials , 1 (2025).
- [10] D.-F. Shao and E. Y. Tsymbal, Antiferromagnetic tunnel junctions for spintronics, npj Spintronics **2**, 13 (2024).
- [11] T. Jungwirth, X. Marti, P. Wadley, and J. Wunderlich, Antiferromagnetic spintronics, Nature nanotechnology 11, 231 (2016).
- [12] D. Xiong, Y. Jiang, K. Shi, A. Du, Y. Yao, Z. Guo, D. Zhu, K. Cao, S. Peng, W. Cai, et al., Antiferromagnetic spintronics: An overview and outlook, Fundamental Research 2, 522 (2022).

- [13] L. Šmejkal, J. Sinova, and T. Jungwirth, Emerging research landscape of altermagnetism, Physical Review X 12, 040501 (2022).
- [14] L. Šmejkal, J. Sinova, and T. Jungwirth, Beyond conventional ferromagnetism and antiferromagnetism: A phase with nonrelativistic spin and crystal rotation symmetry, Physical Review X 12, 031042 (2022).
- [15] S. S. Fender, O. Gonzalez, and D. K. Bediako, Altermagnetism: A chemical perspective, Journal of the American Chemical Society 147, 2257 (2025).
- [16] P. Liu, J. Li, J. Han, X. Wan, and Q. Liu, Spin-group symmetry in magnetic materials with negligible spinorbit coupling, Physical Review X 12, 021016 (2022).
- [17] X. Chen, Y. Liu, P. Liu, Y. Yu, J. Ren, J. Li, A. Zhang, and Q. Liu, Unconventional magnons in collinear magnets dictated by spin space groups, Nature, 1 (2025).
- [18] L. Bai, W. Feng, S. Liu, L. Śmejkal, Y. Mokrousov, and Y. Yao, Altermagnetism: Exploring new frontiers in magnetism and spintronics, Advanced Functional Materials 34, 2409327 (2024).
- [19] D.-F. Shao, S.-H. Zhang, M. Li, C.-B. Eom, and E. Y. Tsymbal, Spin-neutral currents for spintronics, Nature Communications 12, 7061 (2021).
- [20] C. Song, H. Bai, Z. Zhou, L. Han, H. Reichlova, J. H. Dil, J. Liu, X. Chen, and F. Pan, Altermagnets as a new class of functional materials, Nature Reviews Materials, 1 (2025).
- [21] V. Baltz, A. Manchon, M. Tsoi, T. Moriyama, T. Ono, and Y. Tserkovnyak, Antiferromagnetic spintronics, Reviews of Modern Physics 90, 015005 (2018).
- [22] J. Liu, J. Zhan, T. Li, J. Liu, S. Cheng, Y. Shi, L. Deng, M. Zhang, C. Li, J. Ding, Q. Jiang, M. Ye, Z. Liu, Z. Jiang, S. Wang, Q. Li, Y. Xie, Y. Wang, S. Qiao, J. Wen, Y. Sun, and D. Shen, Absence of altermagnetic spin splitting character in rutile oxide ruo₂, Phys. Rev. Lett. 133, 176401 (2024).
- [23] S. Noh, G.-H. Kim, J. Lee, H. Jung, U. Seo, G. So, J. Lee, S. Lee, M. Park, S. Yang, et al., Tunneling magnetoresistance in altermagnetic RuO₂-based magnetic tunnel junctions, Physical Review Letters 134, 246703 (2025).
- [24] O. Fedchenko, J. Minár, A. Akashdeep, S. W. D'Souza, D. Vasilyev, O. Tkach, L. Odenbreit, Q. Nguyen, D. Kutnyakhov, N. Wind, et al., Observation of time-reversal

- symmetry breaking in the band structure of altermagnetic RuO₂, Science advances 10, eadj4883 (2024).
- [25] M. Hiraishi, H. Okabe, A. Koda, R. Kadono, T. Muroi, D. Hirai, and Z. Hiroi, Nonmagnetic ground state in RuO₂ revealed by muon spin rotation, Physical Review Letters 132, 166702 (2024).
- [26] Z. Wu, M. Long, H. Chen, S. Paul, H. Matsuki, O. Zheliuk, U. Zeitler, G. Li, R. Zhou, Z. Zhu, et al., Fermi surface of RuO₂ measured by quantum oscillations, Physical Review X 15, 031044 (2025).
- [27] B. Jiang, M. Hu, J. Bai, Z. Song, C. Mu, G. Qu, W. Li, W. Zhu, H. Pi, Z. Wei, et al., A metallic roomtemperature d-wave altermagnet, Nature Physics 21, 754 (2025).
- [28] R. Sarkar, Altermagnet with a metallic touch, Nature Physics, 1 (2025).
- [29] F. Zhang, X. Cheng, Z. Yin, C. Liu, L. Deng, Y. Qiao, Z. Shi, S. Zhang, J. Lin, Z. Liu, et al., Crystal-symmetrypaired spin-valley locking in a layered room-temperature metallic altermagnet candidate, Nature Physics 21, 760 (2025).
- [30] J. Lai, T. Yu, P. Liu, L. Liu, G. Xing, X. Chen, and Y. Sun, d-wave flat fermi surface in altermagnets enables maximum charge-to-spin conversion, arXiv preprint arXiv:2506.07703 (2025).
- [31] S. H. Simon, The Oxford solid state basics (OUP Oxford, 2013).
- [32] S. Yuasa, T. Nagahama, A. Fukushima, Y. Suzuki, and K. Ando, Giant room-temperature magnetoresistance in single-crystal Fe/MgO/Fe magnetic tunnel junctions, Nature materials 3, 868 (2004).
- [33] S. S. Parkin, C. Kaiser, A. Panchula, P. M. Rice, B. Hughes, M. Samant, and S.-H. Yang, Giant tunnelling magnetoresistance at room temperature with MgO (100) tunnel barriers, Nature materials 3, 862 (2004).
- [34] P.-H. Fu, S. Mondal, J.-F. Liu, and J. Cayao, Lightinduced floquet spin-triplet cooper pairs in unconventional magnets, arXiv preprint arXiv:2506.10590 (2025).
- [35] P.-H. Fu, S. Mondal, J.-F. Liu, Y. Tanaka, and J. Cayao, Floquet engineering spin triplet states in unconventional magnets, arXiv preprint arXiv:2505.20205 (2025).
- [36] S. Datta, *Electronic transport in mesoscopic systems* (Cambridge university press, 1997).
- [37] P. Fu, Q. Lv, Y. Xu, J. Cayao, J. Liu, and X. Yu, Allelectrically controlled spintronics in altermagnetic heterostructures, arXiv preprint arXiv:2506.05504 (2025).
- [38] L. Šmejkal, A. B. Hellenes, R. González-Hernández, J. Sinova, and T. Jungwirth, Giant and tunneling magnetoresistance in unconventional collinear antiferromagnets with nonrelativistic spin-momentum coupling, Physical Review X 12, 011028 (2022).
- [39] H.-Y. Ma, M. Hu, N. Li, J. Liu, W. Yao, J.-F. Jia, and J. Liu, Multifunctional antiferromagnetic materials with giant piezomagnetism and noncollinear spin current, Nature communications 12, 2846 (2021).
- [40] D. Xiao, G.-B. Liu, W. Feng, X. Xu, and W. Yao, Coupled spin and valley physics in monolayers of MoS₂ and other group-vi dichalcogenides, Physical review letters 108, 196802 (2012).
- [41] J. R. Schaibley, H. Yu, G. Clark, P. Rivera, J. S. Ross, K. L. Seyler, W. Yao, and X. Xu, Valleytronics in 2d materials, Nature Reviews Materials 1, 1 (2016).
- [42] X. Xu, W. Yao, D. Xiao, and T. F. Heinz, Spin and pseudospins in layered transition metal dichalcogenides,

- Nature Physics 10, 343 (2014).
- [43] C. Yang, Z. Song, X. Sun, and J. Lu, Valley pseudospin in monolayer MoSi₂N₄ and MoSi₂As₄, Physical Review B 103, 035308 (2021).
- [44] M. Zeng, M.-Y. Zhu, Y.-P. Zhu, X.-R. Liu, X.-M. Ma, Y.-J. Hao, P. Liu, G. Qu, Y. Yang, Z. Jiang, et al., Observation of spin splitting in room-temperature metallic antiferromagnet CrSb, Advanced Science 11, 2406529 (2024).
- [45] S. Reimers, L. Odenbreit, L. Šmejkal, V. N. Strocov, P. Constantinou, A. B. Hellenes, R. Jaeschke Ubiergo, W. H. Campos, V. K. Bharadwaj, A. Chakraborty, et al., Direct observation of altermagnetic band splitting in CrSb thin films, Nature Communications 15, 2116 (2024).
- [46] A. Ablimit, Y.-L. Sun, E.-J. Cheng, Y.-B. Liu, S.-Q. Wu, H. Jiang, Z. Ren, S. Li, and G.-H. Cao, V₂te₂o: A twodimensional van der waals correlated metal, Inorganic Chemistry 57, 14617 (2018).
- [47] K. D. Belashchenko, E. Y. Tsymbal, M. van Schilfgaarde, D. A. Stewart, I. I. Oleynik, and S. S. Jaswal, Effect of interface bonding on spin-dependent tunneling from the oxidized co surface, Phys. Rev. B 69, 174408 (2004).
- [48] K. Samanta, D.-F. Shao, and E. Y. Tsymbal, Spin filtering with insulating altermagnets, Nano Letters 25, 3150 (2025).
- [49] B. Chi, L. Jiang, Y. Zhu, G. Yu, C. Wan, and X. Han, Anisotropic spin filtering by an altermagnetic barrier in magnetic tunnel junctions, Physical Review Applied 23, 014013 (2025).
- [50] Z. Yang, X. Yang, J. Wang, R. Peng, L. C. Hua, L. K. Ang, J. Lu, Y. S. Ang, and S. Fang, Unconventional tunnel magnetoresistance scaling with altermagnets, arXiv preprint arXiv:2505.17192 (2025).
- [51] J. Gong, Y. Wang, Y. Han, Z. Cheng, X. Wang, Z.-M. Yu, and Y. Yao, Hidden real topology and unusual magneto-electric responses in two-dimensional antiferromagnets, Advanced Materials 36, 2402232 (2024).
- [52] S. Fang, Z. Yang, J. Wang, X. Yang, J. Lu, C. H. Lee, X. Wang, and Y. S. Ang, Edgetronics in two-dimensional altermagnets, arXiv preprint arXiv:2508.10451 (2025).
- [53] H. Lin, J. Si, X. Zhu, K. Cai, H. Li, L. Kong, X. Yu, and H.-H. Wen, Structure and physical properties of $CsV_2Se_{2-x}O$ and V_2Se_2O , Physical Review B **98**, 075132 (2018).
- [54] G. Gurung, M. Elekhtiar, Q.-Q. Luo, D.-F. Shao, and E. Tsymbal, Nearly perfect spin polarization of noncollinear antiferromagnets, Nat. Commun 15, 10242 (2024).
- [55] F. Liu, Z. Zhang, X. Yuan, Y. Liu, S. Zhu, Z. Lu, and R. Xiong, Giant tunneling magnetoresistance in insulated altermagnet/ferromagnet junctions induced by spin-dependent tunneling effect, Physical Review B 110, 134437 (2024).
- [56] K. Samanta, Y.-Y. Jiang, T. R. Paudel, D.-F. Shao, and E. Y. Tsymbal, Tunneling magnetoresistance in magnetic tunnel junctions with a single ferromagnetic electrode, Physical Review B 109, 174407 (2024).
- [57] D. Waldron, V. Timoshevskii, Y. Hu, K. Xia, and H. Guo, First principles modeling of tunnel magnetoresistance of Fe/MgO/Fe trilayers, Physical review letters 97, 226802 (2006).
- [58] L. Zhang, G. Ni, J. He, and G. Gao, Above room temperature multiferroic tunnel junction with the altermagnetic

- metal crsb, Physical Review B 112, 064401 (2025).
- [59] S. Liu, T. Chen, B. Wu, H. Fan, Y. Zhu, S. Bi, Y. Liu, Y. Shi, W. Zhang, M. Wang, et al., Mn₃SnN-based antiferromagnetic tunnel junction with giant tunneling magnetoresistance and multi-states: Design and theoretical validation, Advanced Science 12, e02985 (2025).
- [60] B. Chi, L. Jiang, Y. Zhu, G. Yu, C. Wan, J. Zhang, and X. Han, Crystal-facet-oriented altermagnets for detecting ferromagnetic and antiferromagnetic states by giant tunneling magnetoresistance, Physical Review Applied 21, 034038 (2024).
- [61] Q. Cui, Y. Zhu, X. Yao, P. Cui, and H. Yang, Giant spinhall and tunneling magnetoresistance effects based on a two-dimensional nonrelativistic antiferromagnetic metal, Physical Review B 108, 024410 (2023).
- [62] J. Dong, X. Li, G. Gurung, M. Zhu, P. Zhang, F. Zheng, E. Y. Tsymbal, and J. Zhang, Tunneling magnetoresistance in noncollinear antiferromagnetic tunnel junctions, Physical Review Letters 128, 197201 (2022).
- [63] S. Manipatruni, D. E. Nikonov, C.-C. Lin, T. A. Gosavi, H. Liu, B. Prasad, Y.-L. Huang, E. Bonturim, R. Ramesh, and I. A. Young, Scalable energy-efficient magnetoelectric spin-orbit logic, Nature 565, 35 (2019).
- [64] G. Kresse and J. Hafner, Ab initio molecular dynamics for liquid metals, Physical review B 47, 558 (1993).
- [65] G. Kresse and J. Furthmüller, Efficient iterative schemes for ab initio total-energy calculations using a plane-wave basis set, Physical review B 54, 11169 (1996).
- [66] J. P. Perdew, K. Burke, and M. Ernzerhof, Generalized gradient approximation made simple, Physical review let-

- ters 77, 3865 (1996).
- [67] S. L. Dudarev, G. A. Botton, S. Y. Savrasov, C. Humphreys, and A. P. Sutton, Electron-energy-loss spectra and the structural stability of nickel oxide: An LSDA + U study, Physical Review B 57, 1505 (1998).
- [68] V. I. Anisimov, J. Zaanen, and O. K. Andersen, Band theory and mott insulators: Hubbard U instead of stoner i, Physical Review B 44, 943 (1991).
- [69] C. Legein, B. J. Morgan, A. G. Squires, M. Body, W. Li, M. Burbano, M. Salanne, T. Charpentier, O. J. Borkiewicz, and D. Dambournet, Correlated anion disorder in heteroanionic cubic TiOF₂, Journal of the American Chemical Society 146, 21889 (2024).
- [70] S. Smidstrup, T. Markussen, P. Vancraeyveld, J. Wellendorff, J. Schneider, T. Gunst, B. Verstichel, D. Stradi, P. A. Khomyakov, U. G. Vej-Hansen, et al., Quantumatk: an integrated platform of electronic and atomic-scale modelling tools, Journal of Physics: Condensed Matter 32, 015901 (2019).
- [71] M. Brandbyge, J.-L. Mozos, P. Ordejón, J. Taylor, and K. Stokbro, Density-functional method for nonequilibrium electron transport, Physical Review B 65, 165401 (2002).
- [72] A. Williams, P. J. Feibelman, and N. Lang, Green's-function methods for electronic-structure calculations, Physical Review B 26, 5433 (1982).
- [73] S. Grimme, Semiempirical GGA-type density functional constructed with a long-range dispersion correction, Journal of computational chemistry 27, 1787 (2006).